Impact of high-order interactions on the fundamental dynamics of four-wave mixing

Anastasiia Sheveleva, Pierre Colman, J.M. Dudley, Christophe Finot

Impact of high-order interactions on the fundamental dynamics of four-wave mixing

Anastasiia Sheveleva[1],* Pierre Colman[1], John M Dudley[2], and Christophe Finot[1]
[1] *Laboratoire Interdisciplinaire Carnot de Bourgogne, UMR 6303 CNRS-Université de Bourgogne Dijon 21000, France and*
[2] *Institut FEMTO-ST, CNRS 6174 UMR Université de Franche-Comté 25000 Besançon, France*
(Dated: April 23, 2024)

We extend the truncated three wave theory used to describe degenerate four-wave mixing in optical fibers to take into account the impact of higher order harmonic sidebands. Using second order perturbation theory combined with adiabatic elimination, our extended theory preserves the initial framework of three waves description. This allows the subsequent discussion regarding the origin of the non-preservation of Fermi-Pasta-Ulam-Tsingou recurrence. Our analytical results are supported by numerical simulations and experimental observations.

Keywords: Fiber optics, four-wave mixing, Hamiltonian dynamics, perturbative system

I. INTRODUCTION

Wave dynamics in a dispersive medium subject to an intensity-dependent phase shift is governed by the the Nonlinear Schrödinger equation (NLSE) [1] which is one of the seminal equations in science. It can be applied to numerous different domains including hydrodynamics, plasma physics, Bose-Einstein condensates and propagation of light in optical fibers [2–4].

One of the most important NLSE processes at the core of numerous fundamental discoveries and practical applications is the modulation instability (MI) [5, 6] which is manifested in a form of spontaneous or seeded amplification of spectral harmonics [7, 8]. The linear stage of the MI can be described in term of the nonlinear four-wave mixing (FWM) which is characterized by changes during propagation in the fiber in spectral amplitudes and phases of individual harmonics [9–11]. The understanding of this fundamental process has improved after development of an analytical truncated three-wave model operating in terms of conjugate variables [12–14]. This has revealed the recursive dynamics of the FWM referring to the celebrated Fermi-Pasta-Ulam-Tsingou (FPUT) recurrence [15] as well as the existence of different types of energy conversion processes depending on the optical phase.

The experimental demonstration and study of FPUT dynamics in optical fibers has been implemented in [16]. Recently we have developed an original experimental setup allowing to limit waves interactions to only three spectral lines in order to demonstrate experimentally the fundamental FWM process [17]. In this work we have successfully reproduced typical features of the truncated model under various initial conditions. However, we also observed certain deviations from the ideal dynamics, resulting into the slight disturbance of the FPUT cycles over long propagation lengths and the non-conservation of the system's invariants. In particular, the spectrum asymmetry and the value of the system's Hamiltonian are not preserved. In [18], we have revealed that changes in the asymmetry originate from a small generation of the second-order sidebands which are naturally occurring during the MI process. Now we would like to discuss more globally the origins of the FPUT disturbance and non-conservation of its associated Hamiltonian.

Systems subject to perturbations, such as, for instance, the presence of higher order harmonics or propagation loss, undergo qualitative changes in their dynamics [19, 20]. Hence, it was demonstrated that linear losses in optical fibers can cause dissipation of the Hamiltonian which results into breaking of the recurrence cycles [21]. In the present work, we consider participation of the second-order sidebands in the dynamics as a source of dissipation which allows development of the modified FWM model in terms of conjugate variables and discussion of the Hamiltonian dissipation. Following experimental demonstrations evidencing deviation from the ideal three wave mixing, even in the situation where extra sidebands and loss are kept negligible, we improve the accuracy of the idealized model while still retaining the nominal three wave description of the dynamics. It now encompasses the effects of higher order sidebands but keeps the simplicity of nominal idealized model. It serves then as support to discuss the onset of cascaded four wave-mixing, and how the Hamiltonian dynamics is perturbed by the sole presence of extra available photon exchange paths.

* anastasiia.sheveleva@u-bourgogne.fr

II. FUNDAMENTAL FOUR-WAVE MIXING DYNAMICS AND ITS LIMITS

A. Truncated FWM model

Presented in its normalized form, the NLSE reads:

$$i\frac{\partial A(\xi,\tau)}{\partial \xi}+\frac{1}{2}\frac{\partial^2 A(\xi,\tau)}{\partial \tau^2}+|A(\xi,\tau)|^2 A(\xi,\tau)=0, \quad (1)$$

where $A(\xi,\tau)=\psi(z,t)/\sqrt{P_0}$ is the optical field normalized to the average power P_0, $\xi=z/L_{NL}$ - the normalized propagation distance, $\tau=t/\sqrt{|\beta_2|\,L_{NL}}$ is the normalized temporal axis, $L_{NL}=(\gamma P_0)^{-1}$ is the nonlinear length. γ and the β_2 denote the nonlinear Kerr parameter and the second-order dispersion, respectively.

Let us consider that the propagating wave contains only three spectral components which are modeled by ideal delta functions and which are equally spaced by the normalized pulsation $\omega_m=2\pi f_m\sqrt{|\beta_2|/\gamma P_0}$. Then we can substitute the following ansatz $A(\xi,\tau)=A_0(\xi)+A_{-1}(\xi)\exp(i\omega_m\tau)+A_1(\xi)\exp(-i\omega_m\tau)$ (with the carrier frequency omitted) in to the NLSE and write the coupled equations for each spectral harmonic, following the guidelines in [12].

To proceed with this description, we then separate the phases and the amplitudes of each wave $A_i(\xi)=a_i(\xi)\exp(i\varphi_i(\xi))$ which leads to a set of 6 differential equation. Introducing the reduced variables $\eta(\xi)=|a_0(\xi)|^2/\sum_{i=-1}^{1}|a_i(\xi)|^2$ as the relative spectral amplitude, and $\phi(\xi)=\varphi_{-1}(\xi)+\varphi_1(\xi)-2\varphi_0(\xi)$ as the relative spectral phase, we obtain after several simplifications [12]

$$\frac{d\eta}{d\xi}=\frac{dH(\eta,\phi)}{d\phi}=-2\eta\,(1-\eta)\sin\phi \quad (2a)$$

$$\frac{d\phi}{d\xi}=-\frac{dH(\eta,\phi)}{d\eta}=(\kappa-1)+3\eta-(2-4\eta)\cos\phi \quad (2b)$$

η and ϕ form a set of conjugate variables, so the $H(\eta,\phi)$ represents the Hamiltonian of the system:

$$H(\eta,\phi)=2\eta\,(1-\eta)\cos\phi-(\kappa-1)\eta-\frac{3}{2}\eta^2 \quad (3)$$

Since the FWM process depends strongly on the phase-matching conditions between the spectral lines [22], a normalized nonlinear mismatch parameter $\kappa=sgn(\beta_2)(2\pi f_m)^2|\beta_2|/\gamma P_0$ is introduced. Note that we consider that the sidebands at $\pm\omega_m$ are symmetric, e.g. have equal spectral amplitudes, which leads to simplified forms of Eq. (2,3) [12].

Using the description of the system in the reduced variables (η,ϕ), one can display the dynamics on the phase-space plane [20, 23]. Here, we use coordinates $(\eta\cos\phi,\eta\sin\phi)$ and a few typical trajectories are displayed in Fig. 1 (a). This representation allows to conveniently distinguish the dynamics with either bounded or unbounded phases (red and blue lines, respectively).

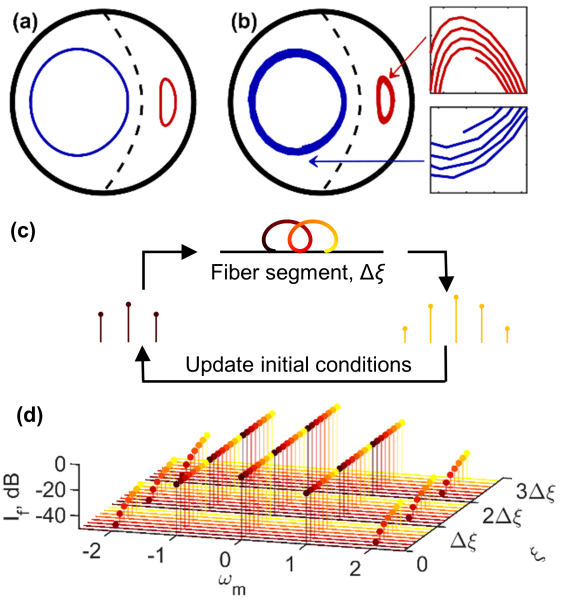

FIG. 1. (a) Fundamental FWM dynamics according to Eq. (2) over $\xi=16$ at $\kappa=-2$, $\eta_0=0.80$ and $\phi_0=0$ and π (red and blue lines, respectively). Black dashed line indicates position of the separatrix. (b) FWM dynamics in a numerical simulation replicating the experiment demonstrates the spiraling dynamics (the simulation parameters are the same as in (a)). (c) Experimental concept where the input conditions are continuously updated after three waves propagated in a small segment of fiber [17]. Bottom panel (d) displays simulated changes in spectral amplitudes during a few consecutive iterations.

These two classes of orbits are divided by an unstable solution at $\eta=1$ and $\phi=\cos^{-1}[-(\kappa+2)/2]$ called the separatrix. In the present paper we will often refer to these two types of dynamics as solutions belonging to the right and the left side of the separatrix.

Such a system, where the dynamics is strictly limited to three spectral lines, is considered as ideal or fundamental four-wave mixing (FWM) in its degenerate case. Here the changes in amplitude and phase follow closed trajectories that are unique for each initial condition and never intersect for a constant κ [24]. Each orbit has its own Hamiltonian (namely energy) value which is preserved during propagation, and represents the conservation of the time-averaged energy of the field. On the extreme positions of the Hamiltonian $\left(\frac{dH(\eta,\phi)}{d\phi}=0,\frac{dH(\eta,\phi)}{d\eta}=0\right)$, there exist stationary solutions which represent waves propagating with no changes neither in the relative phase nor in the relative amplitude [12].

B. Principle of the experimental approach

The experimental demonstration of the fundamental FWM in optical fibers is a rather challenging task. The effects of propagation losses and generation of higher-

order sidebands that naturally occur in the fiber cause deviation from the ideal model and break the FPUT recurrence [18, 25].

In our previous works, we have constructed an original experimental setup aiming to the demonstration of fundamental FWM [17]. The main idea of the experimental approach (displayed in Fig. 1 (c)) was to tailor the input signal's (η_i, ϕ_i) with a programmable spectral filter and then propagate it in a small segment of fiber $\Delta\xi$. After measuring the output parameters (η_{i+1}, ϕ_{i+1}), we update the input conditions; and iterate this process in a loop. This allows to reproduce the ideal FWM dynamics over long propagation distances: over 50 km or $\xi = 12$ at $\kappa = -2$ in a 500-m fiber with $\gamma = 1.7$ (W km)$^{-1}$, $\beta_2 = -8$ ps^{2}km^{-1} of 500 m length.

Such a method allows to exclude the impact of propagation losses and limits generation of the higher-order sidebands at $\pm p\omega_m$ $(p \geq 2)$. After each iteration, we update the parameters of the three central harmonics $(-\omega_m, 0, \omega_m)$, while others are filtered out in the recycling process. Nevertheless, we cannot completely exclude their generation as light propagates in the fiber, and we observe occurrence of the second-order sidebands with a level below 1% of the total spectral intensity. The panel (d) of Fig. 1 showcases a gradual growth of the spectral lines at $\pm 2\omega_m$ which are filtered after each iteration of $\Delta\xi$, so the process starts anew at updated values of (η_{i+1}, ϕ_{i+1}).

The impact of the second-order harmonics is not pronounced over short propagation distances ($<$ 50 km), however, at higher lengths, the accumulation of these small perturbations results in a deviation from the closed orbits.

Such a behavior is presented in Fig. 1 (b), where the signals with the same initial conditions as in Fig. 1 (a) propagate over $\xi = 16$ in the numerical simulation, emulating experimental conditions (segmented propagation according the NLSE with recycling of the three-waves parameters after each $\Delta\xi = 0.128$). We observe that the trajectories indeed do not follow the closed orbits anymore but begin to spiral inwards. Similar behaviour has been observed experimentally: trajectories stay within the same dynamics type (with bounded or unbounded phase) but the FPUT recurrence is not perfectly preserved.

In order to provide an unambiguous explanation for this phenomena that is observed both experimentally and numerically, we develop in the next section a modified theoretical model.

III. DEVELOPMENT OF A MODIFIED FWM MODEL

A. Impact of the second-order harmonics

As soon as their existence is permitted, second-order harmonics are created and interact with the three central lines. This corresponds to the opening of new mixing (i.e. nonlinear scattering) paths for the photons. By adding into Eq. (2) these new mixing possibilities, the observed deviation from the ideal dynamics must then be reproduced.

This would however complexify the theoretical model from two coupled equations to five. That said, the amplitude of the second-order harmonics remains small, and they impact the dynamics only after large propagation distance. Therefore the extended system can be understood as an Hamiltonian (the three central lines) system in weak interaction with a coherent but dissipative reservoir (the second-order harmonics). The equations for second order harmonics can be solved in term of the reduced variables (η, ϕ); and their effects can then be incorporated adiabatically in the nominal system of Eq. (2). In contrast with previous derivations regarding the FWM where the increase of accuracy was made at the cost of the simplicity (one more equation per extra sideband) [9–11, 26], the present demonstration retains the original simplicity of the system.

In detail, to formulate the modified model, we take an approach similar to our previous work where we discussed the non-conservation of the asymmetry invariant in the experimental dynamics [18]. First, the second-order sidebands are growing from noise, and at low values of κ (< -1), the modulation instability gain bandwidth does not include them. As a result they are neither amplified, nor generated efficiently. In this context, we can therefore consider only stimulated processes (see Fig. 6 in the Appendix A) and neglect spontaneous FWM. The mathematical derivation, and the resulting final system of coupled equations for the waves' amplitudes and phases are described in the Appendix A.

For segment $\Delta\xi$ small enough with respect to the characteristic evolution length of the unperturbed FPUT recurrence (defined as a length required to observe one recurrence cycle), the equations governing the evolution of the extra sidebands Eq. (A1) can be integrated to result in the following amplitude for the second-order sidebands:

$$a_{\pm 2} = \frac{\Delta\xi}{4}\sqrt{\eta}(1-\eta)\left[\sin(\varphi_{\pm 2} - \phi) + 2\sin\varphi_{\pm 2}\right] \qquad (4)$$

Note that the transfer of energy to the ± 2 sidebands is a phase-dependent process. Because at the start of each fiber segment $a_{\pm 2} = 0$, their phase may be undefined at first. The maximal growth of the $a_{\pm 2}$ sidebands will actually happen if all the photons are scattered into them with the same phase, resulting in a net coherent accumulation of energy. When the (η, ϕ) vary over a small $\Delta\xi$, this situation corresponds mathematically to $\frac{d\varphi_{\pm 2}}{d\xi} = 0$, which hence gives:

$$\varphi_{\pm 2} = -\tan^{-1}\left(\frac{2+\cos\phi}{\sin\phi}\right) + \pi M \qquad (5)$$

$M = 1$ if $\sin\phi > 0$ and $M = 0$, otherwise.

In a case when spectral lines are amplified from noise in an undepleted pump approximation and $\phi = 0$, we reconstruct the relative phase of $\pm\pi/2$ from Eq. (5) [27–29]. In other cases, this expression gives a correct approximation of the second-order sidebands' phase, which was verified in our numerical simulation of the iterated NLSE propagation.

B. Complete modified model

After solving the equations in a the undepleted pump approximation, the second-order harmonics can be expressed only in term of the reduced variables. Eq. (2) can therefore be complemented by a corrective term involving only the latter, hence we obtain:

$$\frac{d\eta}{d\xi} = -2\eta\,(1-\eta)\sin\phi + \frac{1}{2}\Delta\xi\eta\,(1-\eta)^2\left[(1+\eta)\sin^2(\varphi_{\pm2}-\phi) + 4\eta\sin\varphi_{\pm2}\sin(\varphi_{\pm2}-\phi) + 4(\eta-1)\sin^2\varphi_{\pm2}\right] \tag{6a}$$

$$\frac{d\phi}{d\xi} = (\kappa-1) + 3\eta - 2\,(1-2\eta)\cos\phi + \frac{1}{4}\Delta\xi(1-\eta)\left[\sin(\varphi_{\pm2}-\phi) + 2\sin\varphi_{\pm2}\right]\left[4(3\eta-1)\cos\varphi_{\pm2} + (5\eta-1)\cos(\varphi_{\pm2}-\phi)\right] \tag{6b}$$

Here, the first part of the equation is responsible for the fundamental FWM processes (Eq. (2)) which are preserved in the modified model too. The second part of expressions appears only due to existence of additional stimulated photon mixing processes which leads to the energy exchange with the second-order harmonics with the phase $\varphi_{\pm2}$ given by Eq. (5). Such a simplification of the model is possible only by assuming a perturbative adiabatic growth of the ±2 spectral lines.

Note that Eq. (6) is only valid for short segment lengths $\Delta\xi$, as discussed previously. If $\Delta\xi$ is large, the assumptions on small growth and constant phase are no longer valid which would lead to discrepancies between the model and the segmented NLSE propagation.

To verify our model, we numerically simulate the experimental dynamics by using segmented propagation of the NLSE. We choose the propagation length of $\xi = 30$ (216 segments of $\Delta\xi = 0.128$) which allows to observe a significant spiraling and, hence, benchmark the solutions of Eq. (6). The results are presented in Fig. 2 for initial conditions $\eta_0 = 0.90, \phi_0 = 0$ (panels 1), $\eta_0 = 0.70, \phi_0 = \pi$ (panels 2) and $\eta_0 = 0.995, \phi_0 = \pi$ (panels 3) at $\kappa = -2$ which implies the maximum modulation instability gain for the ±1 sidebands.

We note a very good agreement of the numerical results and our modified model especially at early stages of propagation. Further dynamics starts to deviate from numerical predictions which can be explained by: a) accumulation of inaccuracies that arise from analytical assumptions regarding $\varphi_{\pm2}$ and the processes included; b) by the fact that η tends to decrease with distance which means that the sidebands are becoming stronger and starting to act as two pumps symmetrically located with respect to the central frequency which ultimately leads to development of additional photons exchange processes not included in our model (this would correspond to the growth of third-order harmonics and could be in some extend related to the discussion in [13]). The accumulation of these effects can ultimately break the recurrence when the trajectory passes nearby the unstable solution which leads to the separatrix crossing as it is depicted in panels 3 of Fig. 2.

IV. STATISTICAL PROPERTIES AND HAMILTONIAN DISSIPATION

As demonstrated in the previous section, the system follows spiraling trajectories gradually, away from the initial closed orbits. This behaviour could be explained by the fact that there may exist global attractors on the phase-space plane, and that the dynamics is impaired by dissipation. Therefore, the next question is to investigate statistical properties of the dynamics and redefine the Hamiltonian.

A. Statistical estimation of attraction regions

To define the attraction regions, we run both the numerical simulation and the developed theoretical model over very long propagation distance $\xi = 255$ on the grid

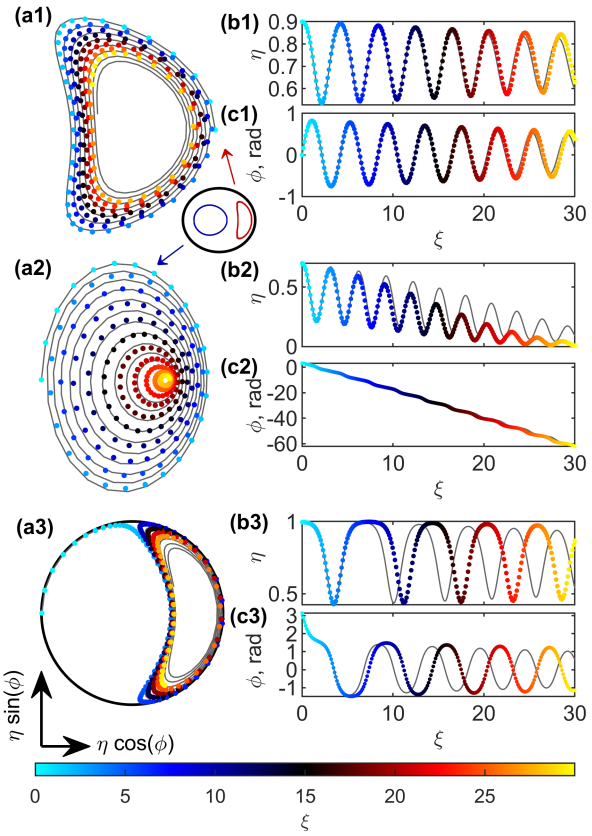

FIG. 2. FWM dynamics according to: numerical simulations (solid lines) and the modified model Eq. (6) (colored points). The inset subplot shows positions of each trajectory on the phase-space map and solutions according to the ideal truncated model. Input parameters are $\eta_0 = 0.90, \phi_0 = 0$ (panels 1), $\eta_0 = 0.70, \phi_0 = \pi$ (panels 2) and $\eta_0 = 0.995, \phi_0 = \pi$ (panels 3) at $\kappa = -2$, $\Delta\xi = 0.128$. Cases (a), (b) and (c) display evolution on the phase-space plane, changes in the relative amplitude η and phase ϕ with propagation distance, respectively.

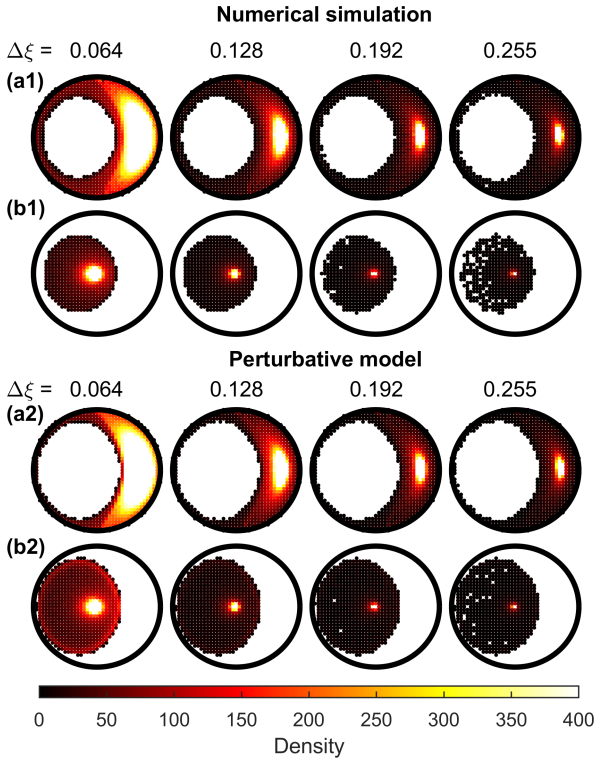

FIG. 3. Density of convergence towards left and right-side stationary solutions (panels (a) and (b), respectively) computed by numerically iterated NLSE propagation (panels 1) and the modified FWM model (panels 2) at $\kappa = -2$.

covering the full phase-space. It gives 112 trajectories which allows to conclude about the number and loci of the attractors, and their respective basins of attraction characterized by the density parameter. It is defined by incrementing the count on the phase-space map's grid when each segment of each trajectory passes by. Since one of the parameters defining the dynamics in our system is the segment length, we repeat the simulation at different values of $\Delta\xi = \{0.064, 0.128, 0.192, 0.255\}$.

Firstly, the data reveal that there exist two well-defined attractors - one on each side of the separatrix. In Fig. 3 we display two families of initial conditions which are attracted to the left and the right-side attractors (panels (a) and (b), respectively) depending on their position on the phase-space map. The density parameter tells how fast a given input configuration would be attracted (the lower value, the faster). We see that attraction is much stronger for large $\Delta\xi$. Moreover, the separatrix between the right and left attractors now differs from the ideal case. In particular, the cycle $\eta = 1$ now belongs exclusively to the right attractor.

With the data presented in Fig. 3, we can benchmark the performance of our model by comparing statistical properties of trajectories computed with the segmented NLSE propagation (panels 1) and with the Eq. (6) (panels 2). We see that both methods provide similar results, and the dependence of the trajectories density at different segment lengths is reproduced correctly. When the segment length is increased, the attraction region on the right side reduces, which can be explained by a more rapid change of parameters during each segment propagation so the spiraling does not appear so gradual.

Secondly, we mark in Fig. 4 (a) the positions of the attractors on the energy landscape defined by the system's Hamiltonian. We see that they are located in the very vicinity of its extreme values: the yellow square shows the exact fixed point $(\eta_{fp} = 0.7143, \phi_{fp} = 0)$ at $\kappa = -2$, while the green dot displays the attractor at $\Delta\xi = 0.128$ which corresponds to the segment length that was investigated experimentally [17]. The extreme point on the left side at $\eta_{fp} = 0$ coincides perfectly with the fixed point of the ideal TWM system.

Details of the right-side attractor also confirm the importance of the stationary point. Even if the exact location very slightly differs from η_{fp}, it remains in the close vicinity from the expected value. In more details,

the relative amplitude and phase values of the attractor are found to be $\eta_a = \{0.7159, 0.7143, 0.7144, 0.7144\}$ and $\phi_a = \{0.0156, 0.0312, 0.0469, 0.0625\}$ rad for $\Delta\xi = \{0.064, 0.128, 0.192, 0.255\}$ corresponding to red, blue and magenta dots in Fig. 4 (a), respectively. We may, however, note a slightly more pronounced change in the relative phase of the attractor that tends to increase with the segment length.

Depending on the starting point, each trajectory converges to the attractors at different rate, hence, it takes different propagation distance before the waves are transformed to the stationary solutions. Dependence of the convergence length (defined as length at which η is close to η_a and the relative change after the consecutive iteration is smaller than 0.01) on the position on the phase-space plane is depicted in Fig. 4 (b).

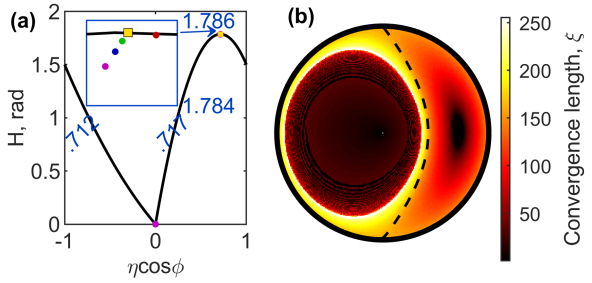

FIG. 4. (a) Attractors of the spiraling dynamics at different segment lengths $\Delta\xi$ are displayed on the Hamiltonian profile at $\kappa = -2$. Yellow square - fixed point $\eta_{fp} = 0.7143, \phi_{fp} = 0$, colored circles - correspond to $\Delta\xi = \{0.064, 0.128, 0.192, 0.255\}$ (red, green, blue and magenta). (b) Convergence length for each initial condition on the phase-space map at $\kappa = -2$ and $\Delta\xi = 0.128$. Black dashed line indicates the separatrix position.

We observe that the total propagation lengths required to converge to each attractor differ significantly. Trajectories on the right tend to have gradually decreasing convergence length when located closer to the attractor, while on the left side of the separatrix there is a region with short and almost homogeneous convergence lengths surrounded by a ring with much higher convergence lengths. In fact, this set of initial conditions converges not to the left, but to the right-side attractor by crossing the separatrix as it is depicted in Fig. 3. In other words, the convergence basins are not exclusively defined by the separatrix. As demonstrated and discussed in [18], growth of the second-order sidebands is not homogeneous on the phase-space map, but more pronounced on the right side of the separatrix. So when an initial condition corresponds to high pump energy on the left side, the contribution of the sidebands into the dynamics is minimal, so the trajectory follows the separatrix closely to a position where the second-order sidebands start to play a more significant role. Since the separatrix is an unstable solution, this small perturbation results into a change in the type of dynamics. So the trajectory can now cross the separatrix and gradually converge to the right-side attractor. Such a case is depicted in panels 3 of Fig. 3.

B. Dissipation of the Hamiltonian and its impact on the FWM

As it was discussed in the previous section, the very existence of additional paths of photons interaction, represented by the higher-order harmonics, leads to deviation of the FWM dynamics from its ideal model. The developed model has shown that the second-order sidebands act as perturbations disrupting the fundamental dynamics which leads to changes in the Hamiltonian profile. The Eq. (6) do not form an Hamiltonian expression, however we can consider a general framework of a Hamiltonian system impaired by dissipation.

In this case, by using the definition of the conjugate variables and splitting functions responsible for the fundamental dynamics $\frac{d\eta}{d\xi} = \frac{dH}{d\phi} = H_\eta$, $\frac{d\phi}{d\xi} = -\frac{dH}{d\eta} = H_\phi$ and the additional terms coming from the second-order harmonics $f_{\delta\eta,\delta\phi}$, one obtains:

$$\frac{d\eta}{d\xi} = H_\eta + f_{\delta\eta} \tag{7a}$$

$$\frac{d\phi}{d\xi} = H_\phi + f_{\delta\phi}. \tag{7b}$$

Then we take a total derivative of the Hamiltonian which reads:

$$\frac{dH}{d\xi} = \frac{\partial H}{\partial \xi}\frac{\partial \xi}{\partial \xi} + \frac{\partial H}{\partial \eta}\frac{\partial \eta}{\partial \xi} + \frac{\partial H}{\partial \phi}\frac{\partial \phi}{\partial \xi}. \tag{8}$$

Now we can substitute the Hamiltonian derivatives by the expressions coming from the ideal model and derivatives of η and ϕ by the modified expressions Eq. (7). Since the unperturbed Hamiltonian does not change during propagation $\frac{\partial H}{\partial \xi} = 0$, the dissipation of the Hamiltonian reads:

$$\frac{dH}{d\xi} = H_\eta(H_\phi + f_{\delta\phi}) - H_\phi(H_\eta + f_{\delta\eta}) = H_\eta f_{\delta\phi} - H_\phi f_{\delta\eta} \tag{9}$$

This equation represents changes in the Hamiltonian under the impact of perturbations induced by the second-order harmonics. Fig. 5 (a) shows $dH/d\xi$ portrait on the phase-space map at different values of κ.

Firstly, we observe on the left side of the separatrix that the highest decay rate is located close to $\eta = 0$, hence explaining the uneven spiraling rate that has been observed in this region (dashed white line in Fig. 5 (a1)). On the right side, the decay rate is not as pronounced, and there is a region where the Hamiltonian is actually recovering ($dH/d\xi$ positive), which slows down further the global spiralling that is observed in this region.

Secondly, in Fig. 5 (a1-3), we see that the positions of regions with growth or decay are more or less preserved and do not depend much on either $\Delta\xi$, nor the

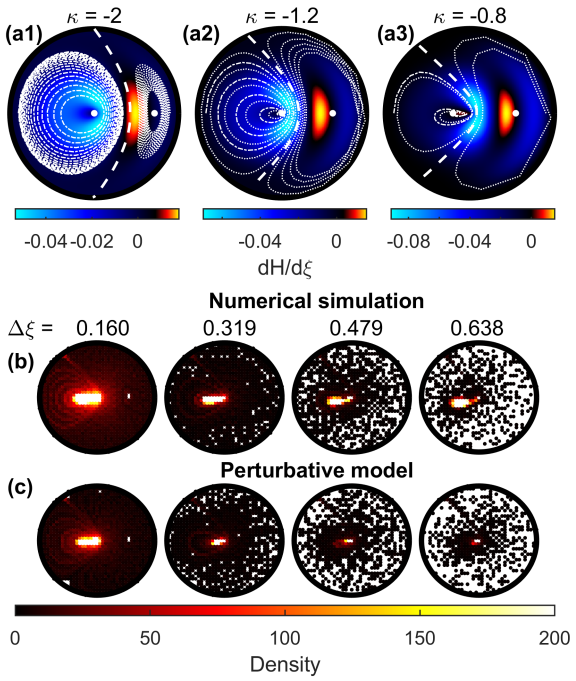

FIG. 5. (a) Distribution of the Hamiltonian dissipation according to Eq. (9) at $\Delta\xi = 0.128$. Thin white dashed and dotted lines correspond to propagation of $\eta_0 = 0.90, \phi_0 = \pi$ and $\phi_0 = 0$, respectively, over $\xi = 60$. Thick white dashed line marks position of the separatrix. White dots denote positions of stationary solutions. (b) Density of convergence towards the fixed point at $\kappa = -0.8$ and different segment lengths $\Delta\xi$.

value of the non-linearity κ. This implies that dissipation mechanism depends mainly on the relation between phases and amplitudes of the pump and the sidebands, but not on type of the dynamics (i.e. with bounded or unbounded phase on the right and left sides of the separatrix, respectively). With growth of κ (e.g. with higher non-linearity), we observe that dissipation and changes in the Hamiltoninan become more significant. Consequently, the nominal ideal dynamics can be modified significantly enough during a single segment of propagation $\Delta\xi$ that it crosses the separatrix (dotted white lines in panels (a2) and (a3) Fig. 5). Existence of localized regions with high losses also explains the rapid spiraling on the left side after just a half-orbit.

To verify the statistical properties of the systems with higher non-linearity, for instance, $\kappa = -0.8$, we run simulations similar to those in Fig. 4. The results are presented in Fig. 5 (b) and (c) for numerical simulation and our modified model, respectively. We observe now that the system converges only to the fixed point $\eta_{fp} = 0$ on the left side of the separatrix, at any segment length. Even trajectories passing closely to the right-side fixed point ($\eta_{fp} = 0.543, \phi_{fp} = 0$) converge to the left side. Such a behavior denotes a complete change of the dynamics (transition from two stable fixed points to only one).

Thirdly, we can now justify why the system is spiraling to the fixed points. From the distributions, presented in Fig. 5 (a), we see that the fixed points (marked as white dots) are located at zero-dissipation values and extremes of the Hamiltonian energy. On the left side, the dissipation is of negative value and the fixed point is a minimum of energy, hence forming a stable attractor (as in the Fig. 5 (a1) and (a2)). In contrast, on the right side of the separatrix, the fixed point is located in between the growth and decay regions, hence forming a saddle point. Therefore, this fixed point becomes gradually more and more unstable as the non-linearity (i.e. $1/|\kappa|$) is increased (as in the Fig. 5 (a3)).

V. DISCUSSION

In previous works, the differences between the evolution of the idealized FWM model and of a real fiber system were attributed to gradual depletion of energy located inside the three central harmonics which is linked to the cascade of the FWM events. In the present work, we can trace the origin of the observed divergences to the very existence of the second-order harmonics. While they carry little energy, the resulting dynamics may differ significantly from the ideal model.

This study bridges a gap between the ideal system where only three spectral lines participate in the dynamics [12, 14] and the full-spectrum wave-mixing during the MI dynamics [30]. The modified model Eq. (6) provides a quantitative description of the cumulative impact of the higher-order sidebands. It can be relevant for systems undergoing parametric wave mixing [26, 29] and for explaining spontaneous FPUT breaking in optical fibers. Furthermore, we discuss a method to include the higher-order sidebands into an intrinsically three-waves dynamics, which can help to describe the spatial Benjamin-Feir instability where the second-order harmonics are linearly stable [31].

On the left side of the separatrix (or on both, in case of high non-linearity), we observe a full conversion of the pump power to the sidebands at any initial condition. This allows a potential implementation of the gain through losses mechanism [32] in our experimental configuration. Indeed, it has been demonstrated that by introducing wavelength-dependent distributed losses [33] or chain of filters [32] one can induce an optical gain that results in a new type of MI [34] or more efficient signal amplification during the FWM process [35]. This type of instability is different from the parametric gain occurring at special resonant conditions under effects of periodic variation of power [36] or dispersion [37–39].

VI. CONCLUSION

In the present work, we demonstrate that the very existence of photons exchange paths with the higher-

order harmonics can lead to disturbance of the fundamental FWM dynamics. We have investigated the non-conservation of the truncated FWM dynamics under a perturbative impact of the second-order sidebands. We have developed a modified model in terms of conjugate variables where some additional photon interaction paths are included, which allows more precise description of the experimental dynamics observed in [17, 18]. The discussions around the Hamiltonian dissipation has allowed to define the origin of this new type of dynamics and explain the spiraling behavior of the trajectories. Before, it has been shown that the linear fiber losses can induce variations of the Hamiltonian [21]. Now we demonstrate that impact of the second-order harmonics can be considered as a perturbation which leads to appearance of Hamiltonian dissipation with positive or negative signs. This approach can be generalized to any system subject to perturbations.

Similarly to nonlinear fiber optics, deep water waves propagation in hydrodynamics can be described by the NLSE, so we can make a link between dissipation in these systems. The waves propagating in a water tank are impaired by frictions and viscosity which impacts the FPUT recurrence [40] and can lead to change of the dynamics type. In the deep water approximations, the perturbations can be caused by the effects of damping and forcing [41] which ultimately leads to the separatrix crossing and change of the dynamics [19, 20]. In our case, even though the nature of dissipation is different, it can still however be considered as a system impaired by a factor external to the truncated three-waves system which is an exchange of photons with higher order harmonics. Therefore, such an approach can be applied to other dynamics which allows to achieve a more accurate description while retaining a simple analytical model.

Our approach relies on adiabatic elimination by assuming a constant phase and an averaged spectral amplitude of the second-order harmonics over each fiber segment, which, on the one hand, allows a simple analytical formulation of the modified equation but, on the other hand, is valid only for a short segment of fiber. A complementary approach for the case of longer fiber segment would be to identify the relevant distributed model by mean of data-driven techniques aiming in the identification of nonlinear dynamics [42].

This work can be also used to gain an understanding and develop new types of fiber-optic parametric amplifiers. Indeed, filtering out the second-order harmonics at each iteration allows conversion between states that are not located on the same trajectory. Our work, which encompasses a complete study on how the dynamics is affected by different initial conditions and introduces the Hamiltonian analysis, can improve understanding on how such systems are affected by asymmetric losses.

ACKNOWLEDGMENTS

The work was funded by the Agence Nationale de la Recherche (Optimal project-ANR-20-CE30-0004; I-SITE-BFC-ANR-15-IDEX-0003), the Région Bourgogne-Franche-Comté and the Centre National de la Recherche Scientifique (MITI interdisciplinary programs, "Evenements extrêmes").

[1] G. P. Agrawal, *Nonlinear Fiber Optics*, 5th ed. (Elsevier Inc., 2013).
[2] B. Kibler, A. Chabchoub, A. Gelash, N. Akhmediev, and V. E. Zakharov, Phys. Rev. X **5**, 041026 (2015).
[3] P. Jha, P. Kumar, G. Raj, and A. K. Upadhyaya, Phys. Plasmas **12**, 123104 (2005).
[4] V. Zakharov and L. Ostrovsky, Phys. D: Nonlinear Phenom. **238**, 540 (2009).
[5] A. Barthelemy and R. De La Fuente, Opt. Commun. **73**, 409 (1989).
[6] F. Copie, S. Randoux, and P. Suret, Rev. Phys. **5**, 100037 (2020).
[7] A. Hasegawa, Opt. Lett. **9**, 288 (1984).
[8] K. Hammani, B. Wetzel, B. Kibler, J. Fatome, C. Finot, G. Millot, N. Akhmediev, and J. M. Dudley, Opt. Lett. **36**, 2140 (2011).
[9] J. R. Thompson and R. Roy, Phys. Rev. A **44**, 7605 (1991).
[10] D. L. Hart, A. Judy, T. A. Brian Kennedy, R. Roy, and K. Stoev, Phys. Rev. A **50**, 1807 (1994).
[11] X. Liu, X. Zhou, and C. Lu, Phys. Rev. A **72**, 013811 (2005).
[12] G. Cappellini and S. Trillo, J. Opt. Soc. Am. B **8**, 824 (1991).
[13] S. Trillo, S. Wabnitz, and T. A. B. Kennedy, Phys. Rev. A **50**, 1732 (1994).
[14] S. Trillo and S. Wabnitz, Opt. Lett. **16**, 986 (1991).
[15] E. Fermi, P. Pasta, S. Ulam, and M. Tsingou, *Studies of nonlinear problems*, Tech. Rep. (Los Alamos National Lab., Los Alamos, NM, 1955).
[16] C. Naveau, G. Vanderhaegen, P. Szriftgiser, G. Martinelli, M. Droques, A. Kudlinski, M. Conforti, S. Trillo, N. Akhmediev, and A. Mussot, Front. Phys. **9**, 637812 (2021).
[17] A. Sheveleva, U. Andral, B. Kibler, P. Colman, J. M. Dudley, and C. Finot, Optica **9**, 656 (2022).
[18] A. Sheveleva, P. Colman, J. M. Dudley, and C. Finot, Ann. Phys. , 2300489 (2024).
[19] A. Armaroli, D. Eeltink, M. Brunetti, and J. Kasparian, Phys. Fluids **30**, 017102 (2018).
[20] D. Eeltink, A. Armaroli, C. Luneau, H. Branger, M. Brunetti, and J. Kasparian, Nonlinear Dyn. **102**, 2385 (2020).
[21] G. Vanderhaegen, P. Szriftgiser, A. Kudlinski, A. Armaroli, M. Conforti, A. Mussot, and S. Trillo, Phys. Rev. A **108**, 033507 (2023).
[22] M. E. Marhic, P. A. Andrekson, P. Petropoulos, S. Radic, C. Peucheret, and M. Jazayerifar, Laser Photonics Rev. **9**, 50 (2015).
[23] S. Trillo and S. Wabnitz, Opt. Lett. **16**, 1566 (1991).

[24] A. Sheveleva, P. Colman, J. M. Dudley, and C. Finot, Opt. Commun. **538**, 129472 (2023).
[25] C. Naveau, P. Szriftgiser, A. Kudlinski, M. Conforti, S. Trillo, and A. Mussot, Opt. Lett. **44**, 5426 (2019).
[26] Y. Chen and A. W. Snyder, Opt. Lett. **14**, 87 (1989).
[27] A. Vatarescu, J. Light. Technol. **5**, 1652 (1987).
[28] M. Marhic, *Fiber Optical Parametric Amplifiers, Oscillators and Related Devices* (Cambridge University Press, 2008).
[29] J. Hansryd, P. Andrekson, M. Westlund, J. Li, and P.-O. Hedekvist, IEEE J. Sel. Top. Quantum Electron. **8**, 506 (2002).
[30] M. Conforti, A. Mussot, A. Kudlinski, S. Trillo, and N. Akhmediev, Phys. Rev. A **101**, 023843 (2020).
[31] C. Heffernan, A. Chabchoub, and R. Stuhlmeier, Nonlinear spatial evolution of degenerate quartets of water waves, arXiv:2403.06558.
[32] A. M. Perego, S. K. Turitsyn, and K. Staliunas, Light Sci. Appl. **7**, 43 (2018).
[33] K. Xu, H. Liu, Y. Dai, J. Wu, and J. Lin, Opt. Commun. **285**, 790 (2012).
[34] T. Tanemura, Y. Ozeki, and K. Kikuchi, Phys. Rev. Lett. **93**, 163902 (2004).
[35] C. Jauregui, A. Steinmetz, J. Limpert, and A. Tünnermann, Opt. Express **20**, 24957 (2012).
[36] F. Matera, A. Mecozzi, M. Romagnoli, and M. Settembre, Opt. Lett. **18**, 1499 (1993).
[37] M. Conforti, A. Mussot, A. Kudlinski, S. Rota Nodari, G. Dujardin, S. De Biévre, A. Armaroli, and S. Trillo, Phys. Rev. Lett. **117**, 013901 (2016).
[38] N. J. Smith and N. J. Doran, Opt. Lett. **21**, 570 (1996).
[39] J. C. Bronski and J. N. Kutz, Opt. Lett. **21**, 937 (1996).
[40] O. Kimmoun, H. C. Hsu, H. Branger, M. S. Li, Y. Y. Chen, C. Kharif, M. Onorato, E. J. R. Kelleher, B. Kibler, N. Akhmediev, and A. Chabchoub, Sci. Rep. **6**, 28516 (2016).
[41] C. Kharif, R. A. Kraenkel, M. A. Manna, and R. Thomas, J. Fluid Mech. **664**, 138 (2010).
[42] A. V. Ermolaev, A. Sheveleva, G. Genty, C. Finot, and J. M. Dudley, Sci. Rep. **12**, 12711 (2022).

Appendix A: Complete set of equations for spectral phases and amplitudes

In order to define the cumulative effect of the second-order sidebands, we include the extra processes that involve generation of the respective spectral lines. Supposing small level of non-linearity ($\kappa < -1$), we can include only photon exchange paths that involve the central lines and one of the sidebands as depicted in Fig. 6.

Considering only symmetric evolution (hence, the asymmetry invariant equals zero [12, 18]), which implies equal changes in phase and amplitude of $+n\omega_m$ and $-n\omega_m$ spectral lines, we can denote spectral amplitudes and phases as $a_{-n} = a_{+n} = a_{\pm n}$ and $\varphi_{-n} = \varphi_{+n} = \varphi_{\pm n}$ $(n = 1, 2)$, respectively. Then the coupled equations presented in [12] are modified as following:

$$\begin{cases} \frac{da_0}{d\xi} = -2a_{\pm1}^2 a_0 \sin(2\varphi_{\pm1} - 2\varphi_0) - 4a_{\pm2}a_{\pm1}^2 \sin(\varphi_{\pm2} - \varphi_0) - 2a_{\pm1}^2 a_{\pm2} \sin(2\varphi_{\pm1} - \varphi_{\pm2} - \varphi_0) \\ \frac{da_{\pm1}}{d\xi} = -a_0^2 a_{\pm1} \sin(2\varphi_0 - 2\varphi_{\pm1}) - 2a_{\pm2}a_{\pm1}a_0 \sin(\varphi_{\pm2} + \varphi_0 - 2\varphi_{\pm1}) \\ \frac{da_{\pm2}}{d\xi} = -a_{\pm1}^2 a_0 \sin(2\varphi_{\pm1} - \varphi_0 - \varphi_{\pm2}) - 2a_0 a_{\pm1}^2 \sin(\varphi_0 - \varphi_{\pm2}) \end{cases} \tag{A1}$$

$$\begin{cases} \frac{d\varphi_0}{d\xi} = a_0^2 + 4a_{\pm1}^2 + 4a_{\pm2}^2 + 2a_{\pm1}^2 \cos\phi + \frac{4a_{\pm2}a_{\pm1}^2}{a_0} \cos(\varphi_{\pm2} - \varphi_0) + \frac{a_{\pm2}a_{\pm1}^2}{a_0} \cos(\varphi_{\pm2} + \varphi_0 - 2\varphi_{\pm1}) \\ \frac{d\varphi_{\pm1}}{d\xi} = \frac{1}{2}\kappa + 2a_0^2 + 3a_{\pm1}^2 + 4a_{\pm2}^2 + a_0^2 \cos\phi + 4a_0 a_{\pm2} \cos(\varphi_{\pm2} - \varphi_0) + 2a_0 a_{\pm2} \cos(\varphi_{\pm2} + \varphi_0 - 2\varphi_{\pm1}) \\ \frac{d\varphi_{\pm2}}{d\xi} = 2\kappa + 2a_0^2 + 4a_{\pm1}^2 + 3a_{\pm2}^2 + \frac{a_{\pm1}^2 a_0}{a_{\pm2}} \cos(\varphi_{\pm2} + \varphi_0 - 2\varphi_{\pm1}) + \frac{2a_{\pm1}^2 a_0}{a_{\pm2}} \cos(\varphi_{\pm2} + \varphi_0) \end{cases} \tag{A2}$$

Since the energy of three lines is conserved at first approximation, and the accumulated energy in the second-order sidebands remains small, we can denote $a_{\pm1} = \sqrt{(1-\eta)/2}$. Substituting this simplification in Eqs. (A1-A2) and using definition $a_0 = \sqrt{\eta}$, results into:

$$\begin{cases} \frac{da_0}{d\xi} = -(1-\eta)\sqrt{\eta} \sin(2\varphi_{\pm1} - 2\varphi_0) - 2a_{\pm2}(1-\eta) \sin(\varphi_{\pm2} - \varphi_0) - (1-\eta)a_{\pm2} \sin(2\varphi_{\pm1} - \varphi_{\pm2} - \varphi_0) \\ \frac{da_{\pm1}}{d\xi} = -\eta\sqrt{(1-\eta)/2} \sin(2\varphi_0 - 2\varphi_{\pm1}) - a_{\pm2}\sqrt{2(1-\eta)}\sqrt{\eta} \sin(\varphi_{\pm2} + \varphi_0 - 2\varphi_{\pm1}) \\ \frac{da_{\pm2}}{d\xi} = -(1-\eta)/2\sqrt{\eta} \sin(2\varphi_{\pm1} - \varphi_0 - \varphi_{\pm2}) - \sqrt{\eta}(1-\eta) \sin(\varphi_0 - \varphi_{\pm2}) \end{cases} \tag{A3}$$

$$\begin{cases} \frac{d\varphi_0}{d\xi} = 2 - \eta + 4a_{\pm2}^2 + (1-\eta)\cos\phi + \frac{2a_{\pm2}(1-\eta)}{\sqrt{\eta}} \cos(\varphi_{\pm2} - \varphi_0) + \frac{a_{\pm2}(1-\eta)}{2\sqrt{\eta}} \cos(\varphi_{\pm2} + \varphi_0 - 2\varphi_{\pm1}) \\ \frac{d\varphi_{\pm1}}{d\xi} = \frac{1}{2}\kappa + 2\eta + 3(1-\eta)/2 + 4a_{\pm2}^2 + \eta\cos\phi + 4\sqrt{\eta}a_{\pm2} \cos(\varphi_{\pm2} - \varphi_0) + 2\sqrt{\eta}a_{\pm2} \cos(\varphi_{\pm2} + \varphi_0 - 2\varphi_{\pm1}) \\ \frac{d\varphi_{\pm2}}{d\xi} = 2\kappa + 2\eta + 2(1-\eta) + 3a_{\pm2}^2 + \frac{(1-\eta)\sqrt{\eta}}{2a_{\pm2}} \cos(\varphi_{\pm2} + \varphi_0 - 2\varphi_{\pm1}) + \frac{(1-\eta)\sqrt{\eta}}{a_{\pm2}} \cos(\varphi_{\pm2} + \varphi_0) \end{cases} \tag{A4}$$

Integrating Eq. (A3) over a short segment of fiber $\Delta\xi$ results in Eq. (4). The stationary phase condition for

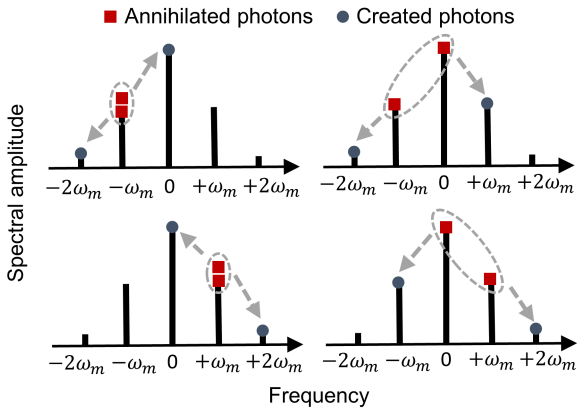

FIG. 6. Possible processes of energy exchange between the three central lines and the second-order sidebands. Spontaneous breaking of a pair of pump photons into +2 and −2 sidebands is negligible in comparison to the others processes which are the stimulated ones.

the second-order harmonics $\frac{d\varphi_{\pm 2}}{d\xi} = 0$ applied to Eq. (A4) results into Eq. (5).